Research article

An integrated global and local thresholding method for segmenting blood vessels in angiography

Min Zhang [a,1], Jun Wang [a,1], Xinhua Cao [b], Xiaoyin Xu [c], Jie Zhou [d], Huai Chen [e,*]

[a] College of Computer Science and Technology, Zhejiang University, Hangzhou, Zhejiang, China
[b] Department of Radiology, Boston Children's Hospital, Boston, MA, 02115, USA
[c] Department of Radiology, Brigham and Women's Hospital, Boston, MA, 02115, USA
[d] Department of Radiology, The First Affiliated Hospital of Guangzhou University of Chinese Medicine, Guangzhou, Guangdong Province, 510405, China
[e] Department of Radiology, The Second Affiliated Hospital of Guangzhou Medical University, Guangzhou, 510260, China

ARTICLE INFO

ABSTRACT

Background: In clinical practice, digital subtraction angiography (DSA) is widely used to diagnose cerebrovascular disease based on detailed information about blood vessel structure. Challenges remain on accurately find blood vessel abnormalities in a time-limited manner. In this perspective, computer-aided analysis of DSA can assist clinicians in interpreting the images.
Purpose: Provide a method for extracting cerebral blood vessels from DSA images.
Materials and methods: In this work, we presented a new method for segmenting digital subtraction angiography (DSA) by incorporating both global and local information about an image to adaptively classify each pixel to the foreground and background. The method utilizes the global mean and standard deviation of an angiography and local mean and standard deviation within a sliding window to build two criteria. The two criteria contains both global and local characteristics about an image and individual pixels. The two criteria work together to reduce noise in segmentation and preserve valid details about the foreground. We tested the method on angiography and compared it with several widely used algorithms.
Results: In total, there were 72 DSA images in our dataset. Compared to Otsu, Niblack, iNiblack, Sauvola, Wolf, and CNW, our method achieved the best overall performance. The accuracy, Dice coefficient (Dice), and intersection over union (IoU) are 0.9777, 0.8500, and 0.7440, respectively.
Conclusion: The results demonstrated that our method can obtain good outcomes, especially in achieving a balance between extracting the correct foreground and reducing incorrect classifications, and had the best performance among the methods being compared with.

1. Introduction

In recent years, due to the improvement of living standards, the incidence of cerebrovascular disease has been rising year by year, posing a great threat to human health [1]. Due to the ability of the DSA to provide detailed information about the vascular structure, it is widely used in clinical practice and considered the gold standard for the diagnosis of cerebrovascular disease [2]. Therefore, a

---

* Corresponding author.
  E-mail address: chenhuai1977@163.com (H. Chen).
[1] Equal contribution.

reliable and automated segmentation of cerebral blood vessels from DSA images is essential [3]. Y. Zhang et al. [4] proposed a method based on the tubular structure of blood vessels. They first used piecewise linear transformations and multi-scale Hessian matrices to enhance the image information, then used gradient-based methods to enhance the blood vessels' edges, and finally employed the Frangi filter to extract the blood vessels. Recently, deep learning networks have shown great potential in vessel segmentation [5–7]. M. Zhang et al. proposed a convolutional neural network (CNN) model based on U-net structure to segment blood vessels in DSA images [8]. Meng et al. [9] presented a multiscale dense CNN model that utilizes the multiscale dilated convolution module to extract features of different cerebrovascular diameters. Due to the difficulty and time-consuming process of labeling blood vessels in DSA images, investigators have recently utilized weakly supervised methods to segment the cerebral blood vessels in DSA images. Vepa et al. [10] proposed the weakly supervised CNN that used the low-cost manual cycle strategy combined with an active contour model to improve the accuracy of segmenting cerebral blood vessels in DSA images.

Segmentation methods generally are of two types, global thresholding and local thresholding. Global thresholding finds and applies a single threshold across the whole image, such as the Otsu method [11] and the integral ratio method [12]. Local thresholding is often adaptive and calculates a threshold for each pixel using some localized information, such as some statistics from a neighborhood of the pixel, such as the Niblack method [13], the Sauvola method [14], the adaptive binarization method by Gatos et al. [15], and the statistical model-based gradient thresholding model by Henstock and Chelberg [16].

The two types of methods have their own advantages and limitations. Generally, global thresholding is based on the calculation of statistics measures about the whole image, such as its mean and standard deviation. A threshold is then built upon the global statistics. An advantage of such methods is that the global statistics are generally robust and unlikely to be affected by noise in the image. Another advantage of global thresholding is that the methods may be parameter-free such as Otsu method [11] which looks for maximizing inter-class variation, though there are global thresholding methods requiring parameter setting [17]. In finding an appropriate threshold from histogram, entropy has been proposed as a criterion for selecting the appropriate threshold. An algorithm based on computing the entropy of each class to maximize the information between two segmented classes was also developed [18]. To incorporate both gray level occurrence and spatial distribution probability, a gray-level and gradient-magnitude (GLGM) histogram has been proposed for finding a segmentation threshold [19]. In this method, the GLGM histogram uses Fibonacci quantized gradient magnitude to capture the spatial information after the image has been pre-processed by anisotropic diffusion in which the user needs to select contrast factor that controls the level of diffusion. A method incorporating 2D histogram information has been developed to maximize the Tsallis entropy in multimodal segmentation [20]. For images with multi-modal histograms, a fuzzy measure method has been presented to first establish a fuzzy region in a histogram and then calculate the similarity between gray levels located within the fuzzy region to assign them to one of the classes [21]. Agrawal et al. [22]presented a multilevel global thresholding method by calculating and minimizing the image entropy along the diagonal regions of its gray level co-occurrence matrix.

Local thresholding techniques such as Niblack method [13], Sauvola method [14], Wolf method [23], and contrast adaptive thresholding method by Feng et al. [24] scan over an image to determine a threshold for every single pixel. Wolf's method normalizes the contrast and the mean gray value of the image to compute an adaptive threshold [23]. For many local thresholding methods, the threshold is not determined a priori but rather on the fly, as such, the threshold is adaptively calculated. For this reason, parameter setting is often involved in local thresholding. The essence of local thresholding is that the segmentation of a pixel is only determined by the neighboring pixels in a small window around the pixel under consideration. As such, information from pixels outside the window, regardless of its usefulness, is not included in segmenting the pixel under consideration. This can be both advantageous and disadvantageous in applications. Often, local adaptive thresholding is sensitive to the pixel intensity distribution in the window, which is an advantage, but this advantage may become a disadvantage when the window contains noisy pixels or interfering structures [25].

In addition, there are other techniques such as level set-based algorithms. For example, K. Zhang et al. [26]presented a method to segment images in the presence of intensity inhomogeneity. Their method uses local statistics to map pixels in a window to a new domain such that intensity probability distributions of different classes of pixels have a reduced overlapping between them, making the separation of the distributions more robust and accurate. Wang et al. developed a nonlinear adaptive level set method for segmenting images with objects of weak boundaries [27]. A recent work by C. Zhang et al. [28]proposed a quantum-based particle swam optimization method based on 2D fuzzy Fisher criterion for segmenting target signal from navigation images.

In this work, we proposed a method that integrates both global and local information of an angiography image in segmentation. Our method considers both global characteristics of an image and its localized structure. Our motivation for developing the new method was to segment blood vessels in angiography images. Though we initially designed the new method tailoring to blood vessel segmentation, our tests show that the method is applicable to other types of images, as shown in the supplemental materials. In implementation, the method is almost parameter-free except for the only parameter being the size of the sliding window used for calculating local information. Comparisons also showed that the new method can perform better than widely used existing methods.

2. Materials and methods

2.1. Data collection

We applied our method on 72 DSA images. The images were obtained from The Second Affiliated Hospital of Guangzhou Medical University and pre-processed according to the principles of Helsinki Declaration, including removing all identifiable information from the data. Ground truth about the images was created by manual labeling and verified by experienced clinicians.

3. Method

Our complete method consists of a main step of segmentation and a post-processing step of enhancing the final output. Fig. 1 shows an angiography image, which has a dark foreground and a bright background. Challenges are mainly concerned with delineating blood vessels of various sizes without introducing non-blood vessel noise and objects in the segmentation result.

3.1. Main step of segmentation

For the main step, our idea is to design a method that integrates global and local information to classify pixels of an image to the foreground F and background B. At first, F and B are two zero-filled matrices of the same size of the input image. As an angiography image I has a dark foreground on a bright background, the threshold has the form of

IF $I(i,j) < T_1(i,j)$ AND $I(i,j) < T_2(i,j)$

$F(i,j) = 1$

ELSE

$B(i,j) = 1$

END

where

$$T_1(i,j) = \mu_{i,j} - \frac{\sigma_G}{\mu_G}\sigma_{i,j}$$

$$T_2(i,j) = \mu_{i,j} - \frac{\sigma_G}{\sigma_{i,j}}\left(\mu_{i,j} - \mu_G\right)$$

where $\mu_{i,j}$ and $\sigma_{i,j}$ are the local mean and standard deviation defined within a sliding window W, respectively. And μ_G and σ_G are the global mean and standard deviation of the whole image, respectively. The size of W is pre-determined. The motivation behind the design of T_1 is to require that a pixel be darker (less) than the local mean minus a multiplication of the local standard deviation for it to be assigned to F. We can consider $\frac{\sigma_G}{\mu_G}$ as a constant that multiplies the local standard deviation $\sigma_{i,j}$. The behavior of $\frac{\sigma_G}{\mu_G}$ is that, for the same μ_G if an image has a large global standard deviation, then $\frac{\sigma_G}{\mu_G}$ is large. This, in turn, translates to a lower $T_1(i,j)$ for pixel $I(i,j)$ to be less than for it to be assigned to F.

The motivation behind the design of T_2 is that, for pixel $I(i,j)$ to be assigned to F, it must be darker (less) than the local mean plus an adjustment, which can be either positive or negative. The adjustment $\left(\mu_{i,j} - \mu_G\right)$ is positive if the local mean is greater than the global
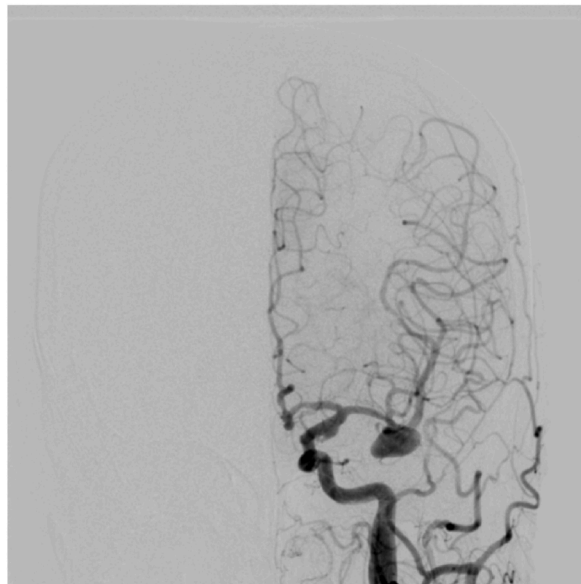

Fig. 1. A. DSA image in coronal view, showing an aneurysm.

mean, meaning that the pixel intensity of the neighborhood is overall greater than the global mean of full image I and, therefore, we require that $I(i,j)$ is less than μ_G minus a positive term to assign it to F, otherwise it is assigned to B. If $\left(\mu_{i,j} - \mu_G\right)$ is negative, then it means the pixel intensity of the neighborhood is overall lower than the global mean of I and we require that $I(i,j)$ be less than a threshold minus μ_G for it to be assigned to F. In both cases, the adjustment is multiplied by a factor $\frac{\sigma_G}{\mu_{i,j}}$, which increases if the local standard deviation $\sigma_{i,j}$ is small, meaning the neighborhood is more homogeneous, and decreases if $\sigma_{i,j}$ is big, meaning the neighborhood is less homogeneous. In other words, when the neighborhood is relatively homogeneous, we require $I(i,j)$ be much lower than μ_G for it to be assigned to F. On the other hand, when the neighborhood is not very homogeneous, we require $I(i,j)$ be lower than μ_G by a lesser extent for it to be assigned to F. By its design, the new method has no parameters except for the size of window W.

To segment an image I that has a bright foreground on a dark background, the new method has the form of

IF $I(i,j) > T_3(i,j)$ AND $I(i,j) > T_4(i,j)$
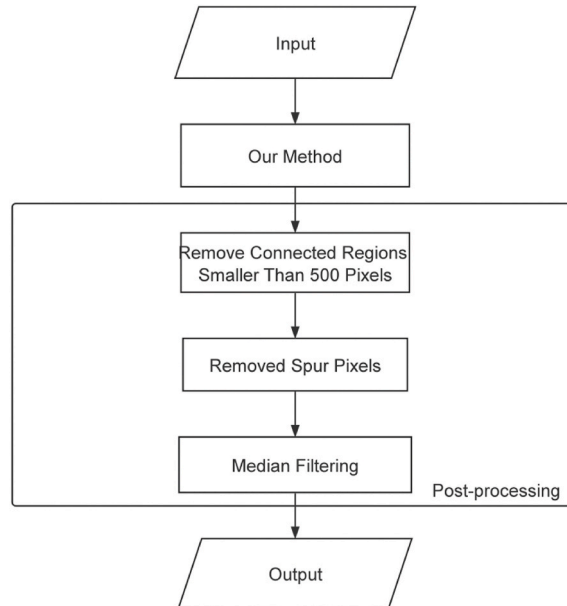
$F(i,j) = 1$

ELSE

$B(i,j) = 1$

END

where $I(i,j)$ is the pixel at position i,j of image I, F and B are the output, and $T_3(i,j)$ and $T_4(i,j)$ are two criteria defined as

$$T_3(i,j) = \mu_{i,j} + \frac{\sigma_G}{\mu_G}\sigma_{i,j}$$

$$T_4(i,j) = \mu_{i,j} + \frac{\sigma_G}{\sigma_{i,j}}\left(\mu_{i,j} - \mu_G\right)$$

The motivation for T_3 and T_4 are similar except they are designed to segment a bright foreground F from a dark background B.

3.2. Post-processing

The result given by the main step may contain noise, spurious protrusions on blood vessels, and some small disconnected objects. As post-processing, to obtain a clear and smoother vascular image, we first removed regions with connected regions of fewer than 500 pixels, then removed spur pixels, and finally smoothed the vessels by median filtering with a 3×3 window size. The flowchart illustration is shown below:

4. Results

We evaluated our method by visual inspection and quantitative metrics. We also assessed the robustness of the method by investigating its performance with various window size k and over different signal-to-background ratio (SBR) of the DSA images.
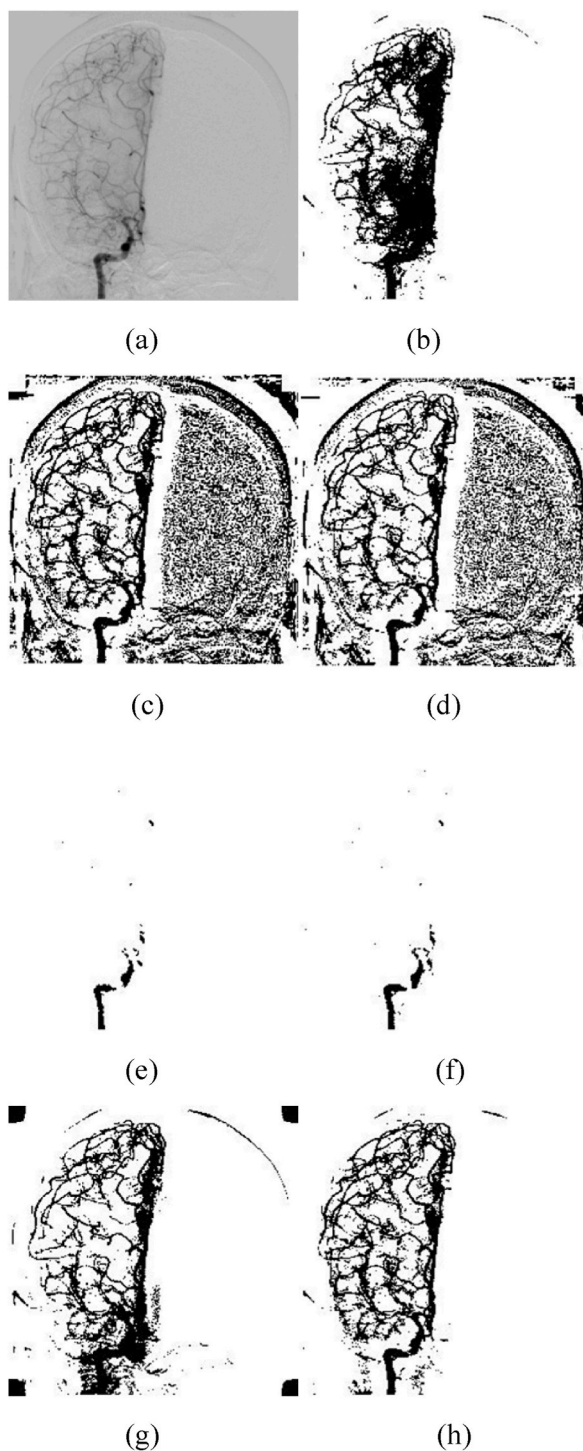

Fig. 2. (a), Original image. (b), Global thresholding result by Otsu method. (c), Niblack result. (d), iNiblack result. (e), Sauvola result. (f), Wolf result. (g), CNW result. (h), Result of the new method without post-processing.
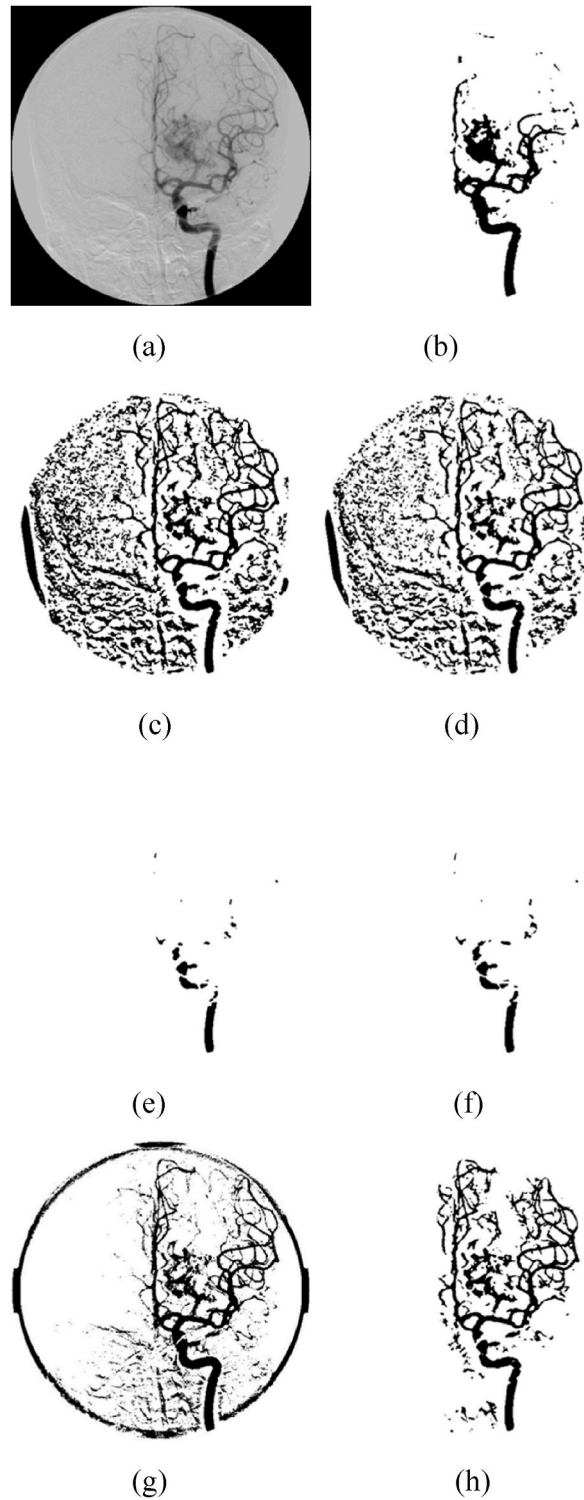
Fig. 3. (a), Original image. (b), Global thresholding result by Otsu method. (c), Niblack result. (d), iNiblack result. (e), Sauvola result. (f), Wolf result. (g), CNW result. (h), Result of the new method without post-processing.

4.1. Visual evaluation of the method

For comparison, we used a global thresholding method, the Otsu method [11], which maximizes inter-group variations, and several local adaptive methods, namely, the Niblack method [13], the Sauvola method [14], the Wolf method [23], the iNiblack method [29], and a method that is a combination of Niblack and Wolf methods [30].
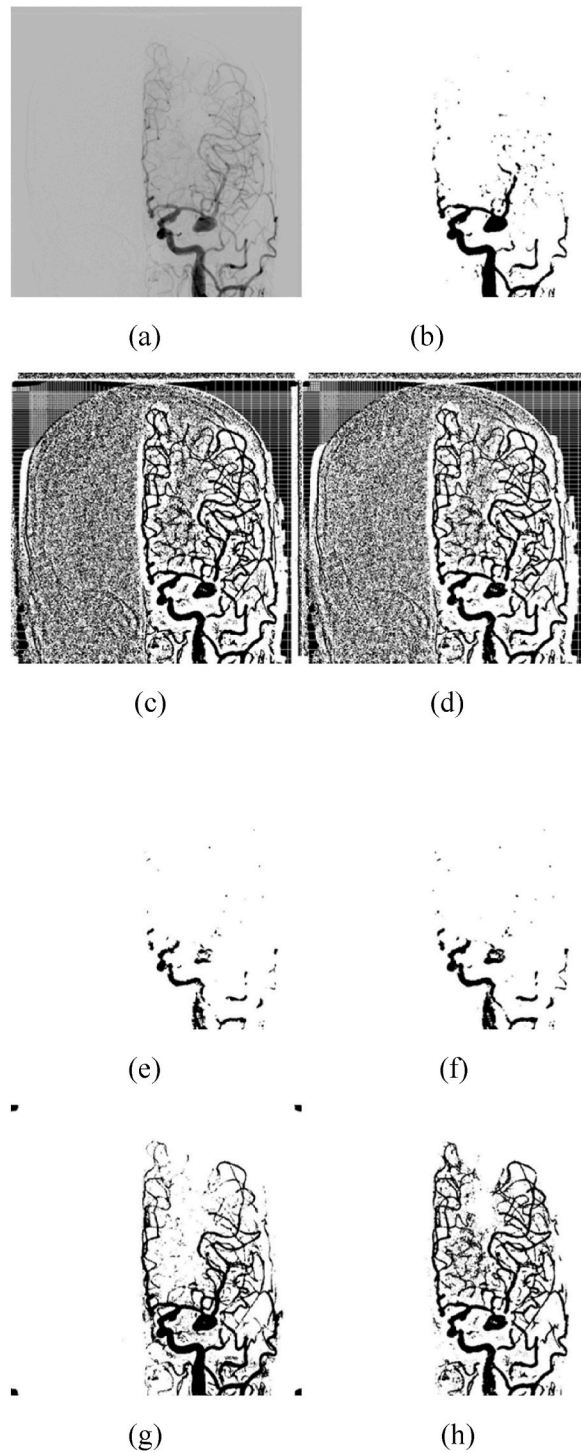

(a) (b)

(c) (d)

(e) (f)

(g) (h)

Fig. 4. (a), Original image. (b), Global thresholding result by Otsu method. (c), Niblack result. (d), iNiblack result. (e), Sauvola result. (f), Wolf result. (g), CNW result. (h), Result of the new method without post-processing.
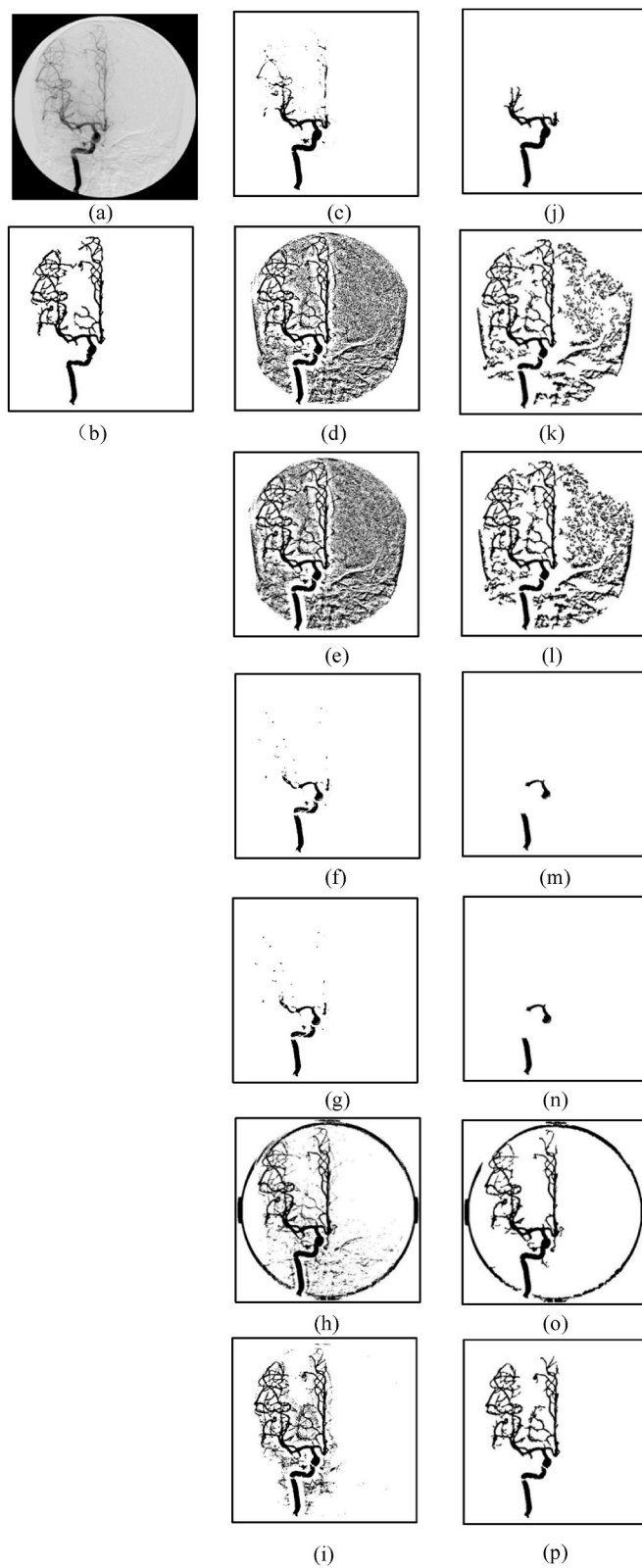
Fig. 5. (a), Original DSA image. (b), Ground truth. (c–i), Results by Otsu, Niblack, iNiblack, Sauvola, Wolf, CNW, and our methods, respectively, without post-processing. (j–p), Corresponding results of (c–i) with post-processing.

In the Niblack method, the local adaptive threshold at position (i, j) is given as

$$T(i, j) = \mu_{i,j} + k\sigma_{i,j}$$

where k is a pre-defined constant and set to -0.2 in Ref. [6]. The size of W is defaulted to 15 in the original design of the method.

The iNiblack method [32] is an extension of Niblack. In the iNiblack method, the k value is determined by the global standard deviation of the image, as

$$k = -\frac{\sigma_G}{255 - 1.5\sigma_G}$$

In the Sauvola method, the local adaptive threshold is given as

$$T(i, j) = \mu_{i,j}\left[1 - k\left(1 - \frac{\sigma_{i,j}}{R}\right)\right]$$

where k is set to 0.5 and R to 128 for images with a pixel intensity in the range of $[0, 255]$.

In the Wolf method, the local adaptive threshold is defined as

$$T(i, j) = (1 - k)\mu_{i,j} + kI_{min} + k\frac{\sigma_{i,j}}{R}\left(\mu_{i,j} - I_{min}\right)$$

where k is a constant set to 0.5, I_{min} is the minimum gray value of I, and R is the maximum of all the local standard deviation

$$R = \max\left[\sigma_{i,j}\right], i = 1, \cdots, M, j = 1, \cdots, N.$$

In a combination of Niblack and Wolf (CNW) methods, researchers proposed a local adaptive threshold defined as

$$T(i, j) = 2\mu_{i,j} + \mu_{i,j}k\left(\left(\sigma_G \big/ \mu_{i,j}\right) - (\sigma_G / R) - 1\right)$$

where k is set to 0.35 in [33]. In this work, k is set to 0.2 as it leads to better results.

4.2. Segmentation without post-processing

At first, we evaluated and compared our method to other methods without any post-processing. In Fig. 2 we show a digital sub-traction angiography (DSA) image. From the original image of Fig. 2(a) we can see that the cerebral blood vessels were of different sizes, ranging from large major arteries to small second-level vessels. The Otsu segmentation is shown in Fig. 2(b). We note that it over-segmented the blood vessels by a large amount. The results of the Niblack and iNiblack methods are shown in Fig. 2(c) and (d), respectively, from which we note that the method over-segmented the image as it generated a large amount of noise in the outcome. The results of the Sauvola and Wolf methods are shown in Fig. 2(e) and (f), respectively, from which we note that they under-segmented the DSA image. The result by CNW method is shown in Fig. 2(g), which consisted of a substantial amount of non-vessel parts. The result of the new method without post-processing, shown in Fig. 2(h), successfully segment the blood vessels and had a small amount of noise in the outcome. With post-processing, noise can be well removed. This example shows that, even without post-processing, our method achieved better performance than existing methods.

Fig. 3(a) shows a second DSA example. Comparing the segmentation given by the seven methods, we note that the Otsu method under-segmented the image as they missed the small blood vessels to the top half of the image, as shown in Fig. 3(b). The Niblack and iNiblack methods, though segmented the blood vessels, generated a large amount of noise, as seen in Fig. 3(c) and (d), respectively. The Sauvola and Wolf methods also under-segmented the image as they missed the small blood vessels to the top half of the image, as shown in Fig. 3(e) and (f), respectively. Fig. 3(g) shows the CNW method has abundant edge noise. The new method gave the best segmentation of the valid cerebral blood vessels, Fig. 3(h). This example again proves that, even without post-processing, our method had the best performance among the methods being compared.

Fig. 4(a) shows a third example of DSA image with an aneurysm (arrow). Comparing the segmentation results by the methods, we note that the Otsu method under-segmented the image, Fig. 4(b). The Niblack and iNiblack methods generated severe over-segmentation, Fig. 4(c) and (d), respectively. Sauvola and Wolf methods under-segmented the image, Fig. 4(e) and (f), respectively. Fig. 4(g) shows the result by the CNW method, which did not find many small blood vessels. The new method gave the best seg-mentation of the valid cerebral blood vessels, Fig. 4(h), while incurring the smallest amount of noise due to the inhomogeneous background of the image. We note that our method and CNW accurately segmented the aneurysm, while the Sauvola and Wolf methods did not segment the aneurysm. We also note that, though Figs. 2(a) and 4(a) were the same type of images, the Otsu method over-segmented Fig. 2(a) and under-segmented Fig. 4(a), pointing to a limitation of global thresholding in such a scenario.

4.3. Segmentation with post-processing

We next evaluated how post-processing can further enhance the performance of the new method. For a fair comparison, we implemented the same post-processing for other methods. Fig. 5 is an example with and without post-processing. Original image and
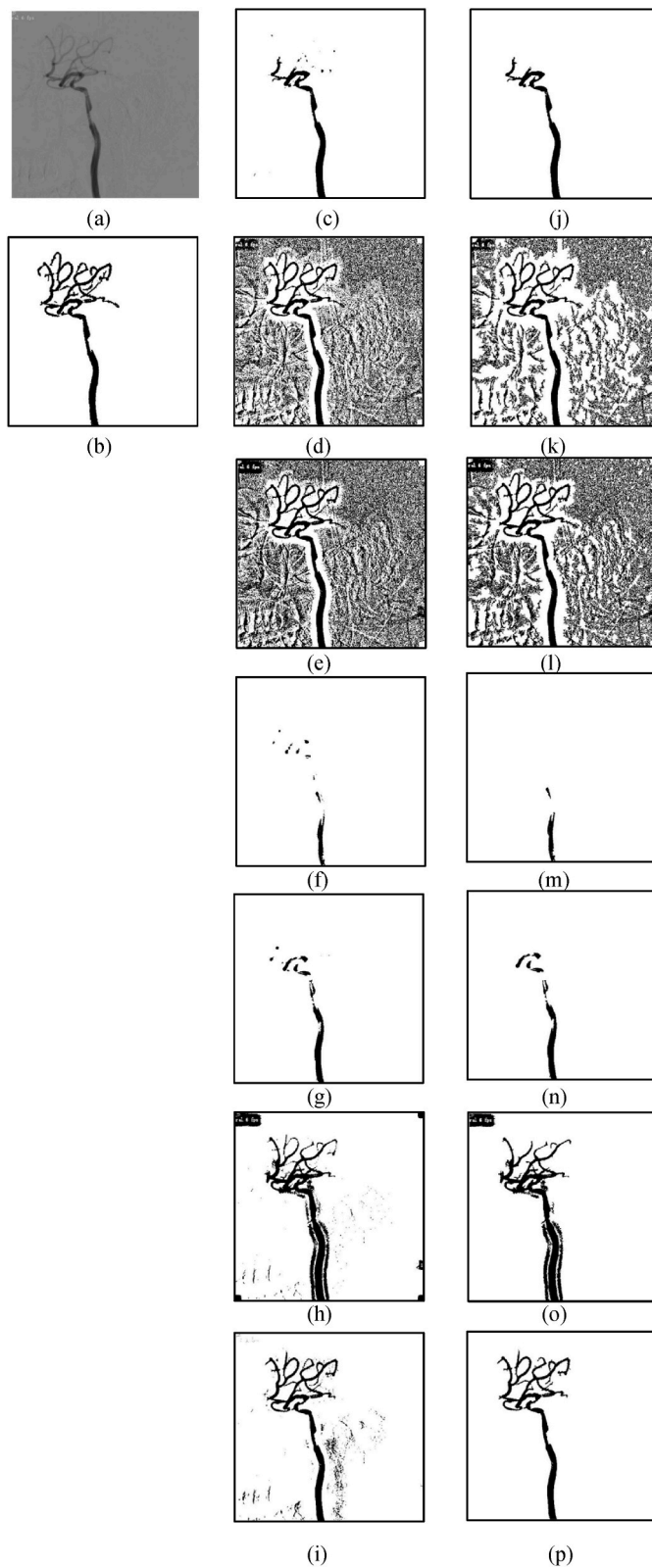
Fig. 6. (a), Original DSA image. (b), Ground truth. (c–i), Results by Otsu, Niblack, iNiblack, Sauvola, Wolf, CNW, and our methods, respectively, without post-processing. (j–p), Corresponding results of (c–i) with post-processing.

Fig. 7. (a), Original DSA image. (b), Ground truth. (c–i), Results by Otsu, Niblack, iNiblack, Sauvola, Wolf, CNW, and our methods, respectively, without post-processing. (j–p), Corresponding results of (c–i) with post-processing.
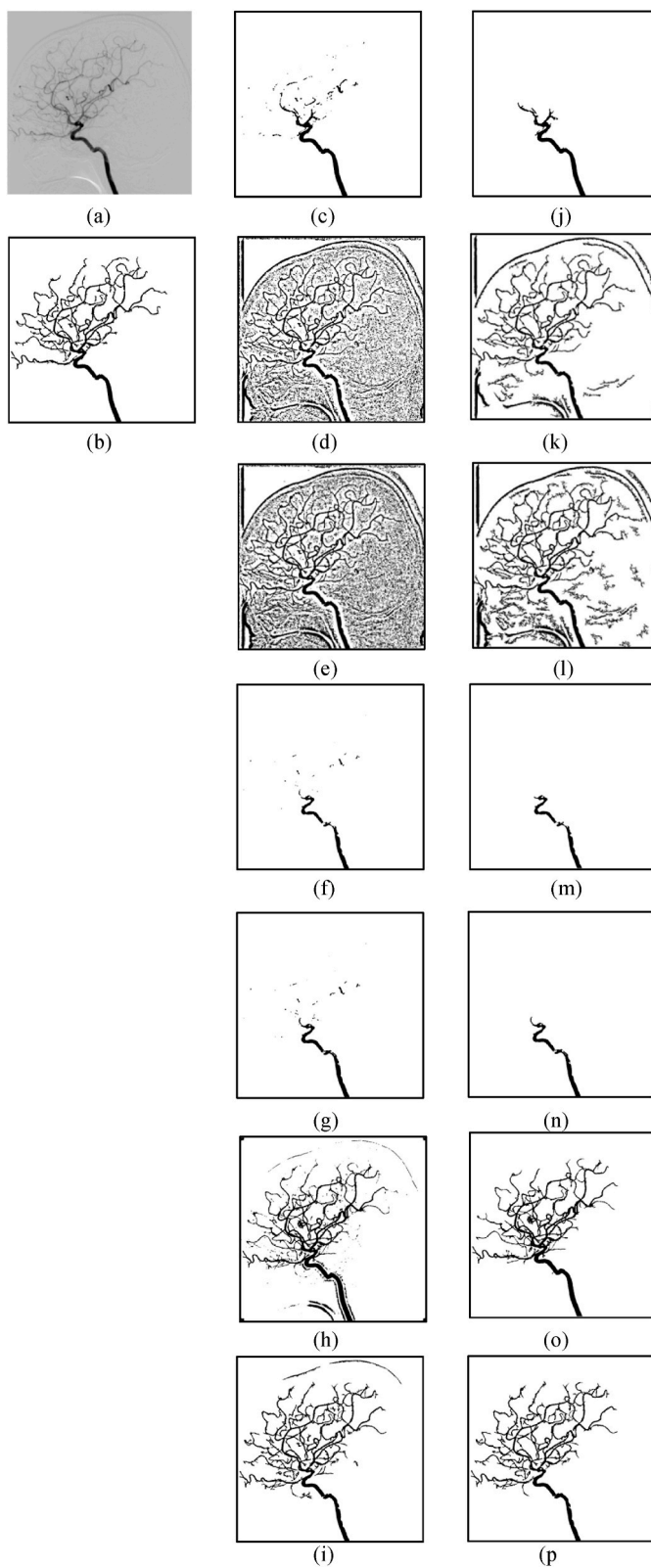
ground truth are shown in Fig. 5(a) and (b), respectively. Fig. 5(c–i) are the segmentation results by the Otsu, Niblack, iNiblack, Sauvola, Wolf, CNW, and our methods, respectively, without post-processing. Fig. 5(j–p) are the corresponding segmentation results with post-processing. We can note that post-processing improved the results by each method while the result by our method, Fig. 5(p), has the cleanest and most accurate depiction of the cerebral blood vessels.

Fig. 6(a) shows another DSA image. Ground truth of the image is shown in Fig. 6(b), from which we note that the DSA image contains a few small second-level vessels. Fig. 6(c–i) are the results by Otsu, Niblack, iNiblack, Sauvola, Wolf, CNW, and our methods, respectively, without post-processing. Fig. 6(j–p) are the corresponding results of Fig. 6(c–i) with post-processing. Comparing the segmentation results with post-processing given by the seven methods, we note that the Otsu, Sauvola, and Wolf methods under-segmented the image while the Niblack, iNiblack, and CNW methods over-segmented the image. The result by our method with post-processing, Fig. 6(p), is the closest to the ground truth and does not contain noise.

Fig. 7(a) and (b) shows a third DSA image and its ground truth. The image contains many small second-level vessels. Fig. 7(c–i) shows the results obtained by Otsu, Niblack, iNiblack, Sauvola, Wolf, CNW, and our methods, respectively, without post-processing. Fig. 7(j–p) are the corresponding results with post-processing. From Fig. 7(i) and (p), we note that our method, with and without post-processing, is able to segment small blood vessels with great accuracy and the whole vasculature as well.

4.4. Quantitative evaluations

For quantitative evaluation, we used accuracy, sensitivity, specificity, Dice coefficient, intersection over union (IoU), and peak signal-to-noise ratio (PSNR). Accuracy, sensitivity, and specificity are defined as follows:

$$\text{Accuracy} = \frac{\text{TP} + \text{TN}}{\text{TP} + \text{FP} + \text{TN} + \text{FN}}$$

$$\text{Sensitivity} = \frac{\text{TP}}{\text{TP} + \text{FN}}$$

$$\text{Specificity} = \frac{\text{TN}}{\text{TN} + \text{FP}}$$

where TP and FP are true positive and false positive, respectively, TN and FN are true negative and false negative, respectively.

Dice coefficient, IoU, and PSNR are defined as

$$\text{Dice} = \frac{2 \times \text{TP}}{2 \times \text{TP} + \text{FP} + \text{FN}}$$

$$\text{IoU} = \frac{\text{TP}}{\text{TP} + \text{FP} + \text{FN}}$$

$$\text{PSNR} = 10 \log\left(\frac{1}{\text{MSE}}\right) \ (\text{dB})$$

where

$$\text{MSE} = \frac{1}{\text{MN}} \sum_{i=1}^{M} \sum_{j=1}^{N} \left(\text{I}'(i,j) - \text{I}(i,j)\right)^2$$

where I$'$ is the segmentation result and I is the ground truth.

Table 1 shows the quantitative comparisons between our method and other methods. Compared to other algorithms, the new method achieved the best results in terms of Dice, IoU, accuracy, and PSNR. The iNiblack and Sauvola methods achieved higher sensitivity and specificity, respectively. However, their other quantitative metrics are much lower than those of our methods. We note that the under-segmentation of the images resulted in low sensitivity for the Otsu, Sauvola, and Wolf methods. Comparing our method

Table 1
Quantitative evaluations with post processing.

Method	ACC	Sn	Sp	Dice	IoU	PSNR
Otsu	0.9491	0.4598	0.9910	0.5716	0.4077	12.64
Niblack	0.9289	0.8412	0.9356	0.6533	0.4946	10.69
iNiblack	0.8953	**0.9393**	0.8912	0.5925	0.4308	10.13
Sauvola	0.9325	0.1394	**0.9992**	0.2344	0.1367	11.17
Wolf	0.9348	0.1753	0.9988	0.2816	0.1710	11.22
CNW	0.9449	0.7844	0.9592	0.6956	0.5441	14.35
Ours	**0.9777**	0.8253	0.9910	**0.8500**	**0.7440**	**15.92**

Note: Acc: accuracy. Sn: sensitivity. Sp: specificity. PSNR is in dB.

to the CNW method, our method had better performance across the board, e.g., the Dice and IoU of our method are 15.44 % and 19.99 % higher than those of the CNW method. Overall, the quantitative results demonstrate that our method achieved the best overall performance among all the methods.

To verify the efficacy of the main step of the new method, we performed an ablation experiment by removing the post-processing part from each method and compared their performance. Table 2 shows the quantitative evaluations without post processing on the same dataset. We can observe that the new method provided the highest performance in Dice, IoU, accuracy, and PSNR. The Otsu, Sauvola, Wolf, and our methods had similar performance with specificity over 97 % and the difference among these methods is very small. The iNiblack and Sauvola methods had better sensitivity and specificity, respectively, but, again, their other metrics were much lower than ours. So these results show that the main segmentation step of our method had better capability than other methods.

4.5. Impact of window size on performance

We note that the only parameter in our method is the window size $(2k + 1) \times (2k + 1)$. In this experiment, we investigated the effect of window size on the performance of our method. We set k to change from 5 to 30 with a step size of 5. Results of this experiment are evaluated by mean Dice coefficient and IoU, as shown in Figs. 8 and 9, respectively. Figs. 8(a) and 9(a), respectively, shows the impact of k values on Dice and IoU of seven methods without post-processing. Figs. 8(b) and 9(b) are the corresponding results with post-processing. We observe that Figs. 8(a) and 9(a) had similar trend. Compared to other algorithms, our method produced the best Dice and IoU when k value was greater than 5. At k = 5, the results of the Otsu, CNW, and our methods were very similar. Due to under-segmentation in Sauvola and Wolf methods and over-segmentation in Niblack and iNiblack methods, the Dice coefficients and IoU of these methods were substantially lower. From Figs. 8(b) and 9(b), we note the Dice and IoU of our method were superior to other methods at all k values, demonstrating not only its accuracy but also its consistency. Our method achieved the best Dice and IoU at k of 15.

Fig. 10 shows how our method with post-processing segmented a DSA image over different k. Original image and ground truth are shown in Fig. 10(a) and (b), respectively. Fig. 10(c–h) are the segmentation results by our method with k at 5, 10, 15, 20, 25, and 30, respectively. Comparing the segmentation results given by the six k values, we note that when the value of k was smaller, our method was able to obtain more small blood vessels, however, the main blood vessels produced some holes in the contrast agent positions, and when the value of k was larger, some small blood vessels are eliminated. On the other hand, the overall vasculature given by our method remained consistent across the window sizes, pointing to an advantage of the method.

4.6. Impact of signal to background ratio on performance

In this experiment, we evaluated the effects of different signal to background ratios (SBRs) on our method. It is important to use SBR to assess the robustness of our method because, in practice, due to the imaging time and amount of dye in the blood vessel, the SBR of DSA may differ. Here, SBR is defined as:

$$SBR = 10 \log_{10} \frac{\mu_s}{\mu_b} \text{ (dB)}$$

where μ_s and μ_b are the average pixel value of the signal and background, respectively. Because in DSA, the signal is darker than the background, a more negative SBR indicates an image of higher contrast in our case. We grouped DSA images by their SBRs into several bins, from −2.4 to −0.6 dB with a bin size of 0.3 dB each. We then calculated the performance of our method for images in each group.

Fig. 11(a) shows the mean Dice coefficients with their variations for different methods without post-processing at various SBRs. Fig. 11(b) is the corresponding results with post-processing. We observe that our method achieved the best mean Dice coefficient and with low variation at each SBR.

Fig. 12 shows a DSA example with and without post-processing results. The SBR of original image, Fig. 12(a), is −2.1 dB, meaning the original image has a comparatively high contrast. Fig. 12(b) is the ground truth. Fig. 12(c–i) are the results by Otsu, Niblack, iNiblack, Sauvola, Wolf, CNW, and our methods, respectively, without post-processing. Dice coefficients of Fig. 12(c–i) are 0.7833, 0.4512, 0.4467, 0.4874, 0.5784, 0.7410, and 0.8528, respectively. Fig. 12(j–p) are the corresponding results of Fig. 12(c–i) with post-processing. Dice coefficients of Fig. 12(j–p) are 0.7188, 0.6081, 0.5926, 0.3391, 0.4144, 0.8450, and 0.8922, respectively. From

Table 2
Quantitative evaluations without post processing.

Method	ACC	Sn	Sp	Dice	IoU	PSNR
Otsu	0.9487	0.5162	0.9862	0.6008	0.4367	12.88
Niblack	0.8193	0.9126	0.8120	0.4547	0.3041	9.48
iNiblack	0.7915	**0.9610**	0.7778	0.4339	0.2869	9.14
Sauvola	0.9349	0.1816	**0.9983**	0.2925	0.1753	11.42
Wolf	0.9373	0.2201	0.9978	0.3431	0.2111	11.53
CNW	0.9250	0.8282	0.9342	0.6463	0.4892	12.71
Ours	**0.9626**	0.8494	0.9730	**0.7838**	**0.6582**	**15.31**

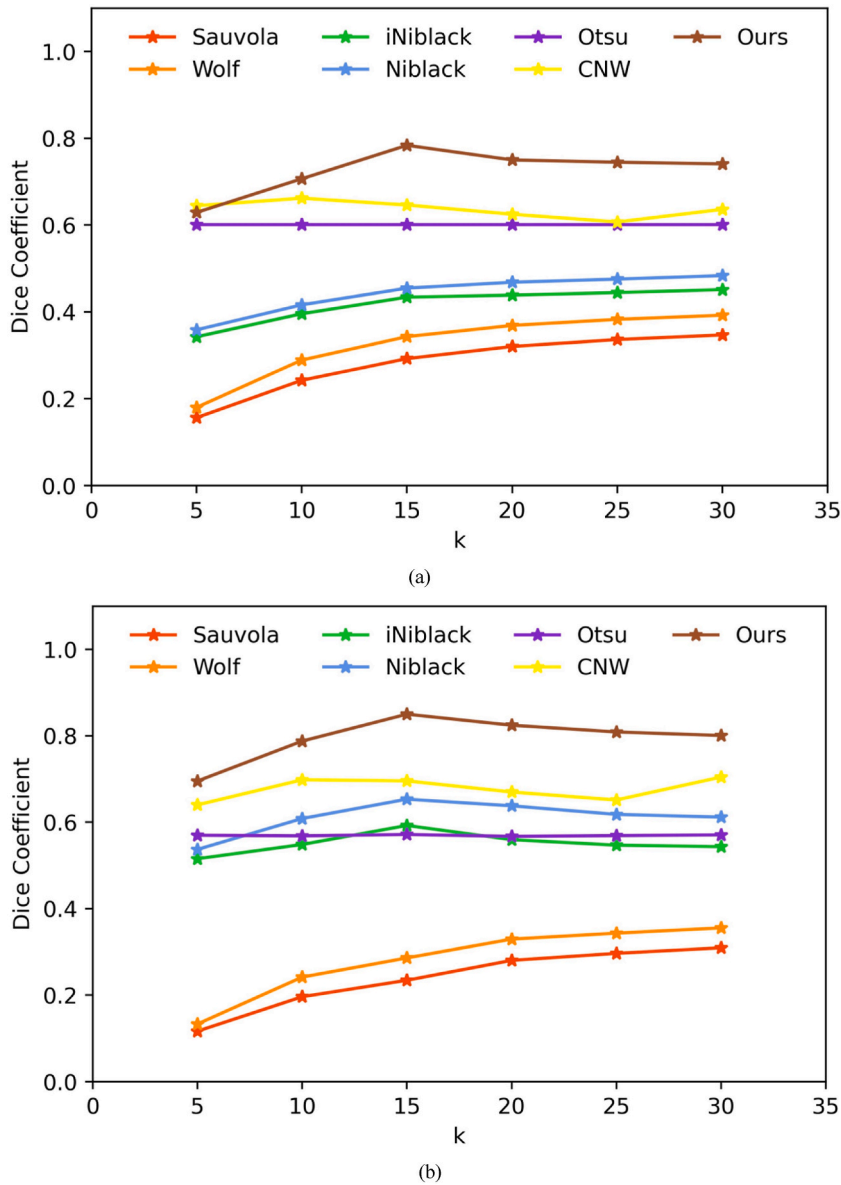Note: Acc: accuracy. Sn: sensitivity. Sp: specificity. PSNR is in dB.

Fig. 8. Impact of window size $W = (2k+1) \times (2k+1)$ on Dice coefficients of different methods. (a), Without post-processing. (b), With post-processing.

Fig. 12(j–n), we note that the Otsu, Sauvola, and Wolf methods under-segmented the image and the Niblack and iNiblack methods over-segmented the image. The CNW method created some noise to the right of the image, Fig. 12(o). Our method, Fig. 12(p), gave the best segmentation of cerebral blood vessels.

Fig. 13 shows another DSA example with and without post-processing results. The SBR value of the original image, Fig. 13(a), is −0.9 dB, meaning this example has a relatively low contrast. Ground truth is shown in Fig. 13(b). Fig. 13(c–i) are the segmentation results without post-processing by the methods. Dice coefficients of Fig. 13(c–i) are 0.3454, 0.3219, 0.2954, 0.2541, 0.2941, 0.5398, and 0.7557, respectively. Fig. 13(j–p) are the corresponding segmentation results with post-processing. Dice coefficients of Fig. 13(j–p) are 0.3121, 0.3798, 0.4469, 0.2066, 0.2783, 0.5038, and 0.8294, respectively. As shown in Fig. 13(p), our method has the most accurate segmentation result at low contrast. These two examples show that our method can maintain a consistent and superior performance over various SBRs, demonstrating its robustness.

4.7. Applicability to other images

The above results demonstrated the effectiveness of our method on segmenting DSA images. The method, nevertheless, is
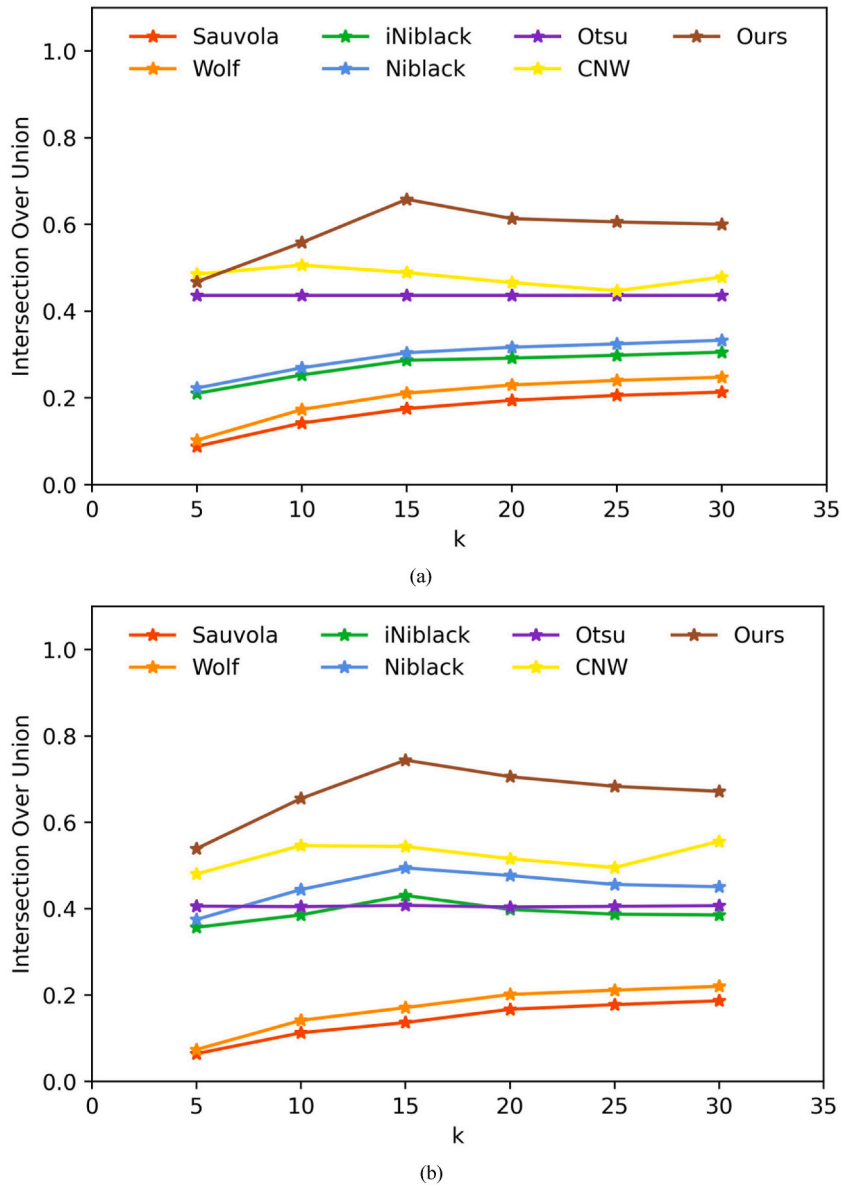
(a)

(b)

Fig. 9. Impact of window size $(2k+1) \times (2k+1)$ on IoU of different methods. (a), Without post-processing. (b), With post-processing.

applicable to other types of images. More examples are given in supplementary materials.

5. Discussion and conclusions

We presented a method incorporating both global and local information for segmenting images. Test results show that the new method can achieve good performance in segmenting DSA. The method, as shown in supplementary materials, is applicable to other types of images, from photographs and microscopic images to scanned documents.

In determining whether a pixel belongs to the foreground or background, the new method requires that the pixel meets two criteria, one is in the global sense and the other in the local sense. The design achieves a good balance between reducing over- and under-segmentation and extracting valid foreground from images. The method takes two forms, one for segmenting images that have a bright foreground on a dark background, and the other for images with a dark foreground on a bright background. The new method is almost parameter-free with the only parameter being the size of the sliding window. Experimental results indicate that the method is robust with the selection of window size.

Innovative contributions of the new method are the judicious integration of global and local features of an image for deriving a highly effective and accurate segmentation approach. The method is shown to have the advantage of global thresholding as being
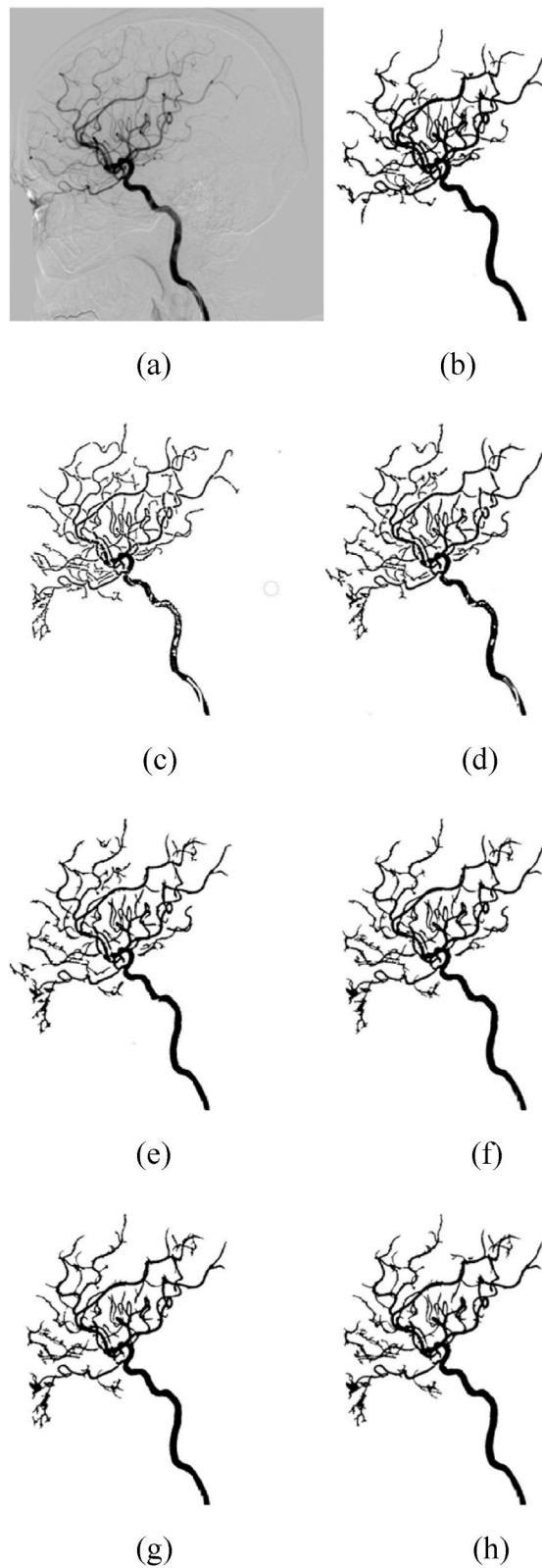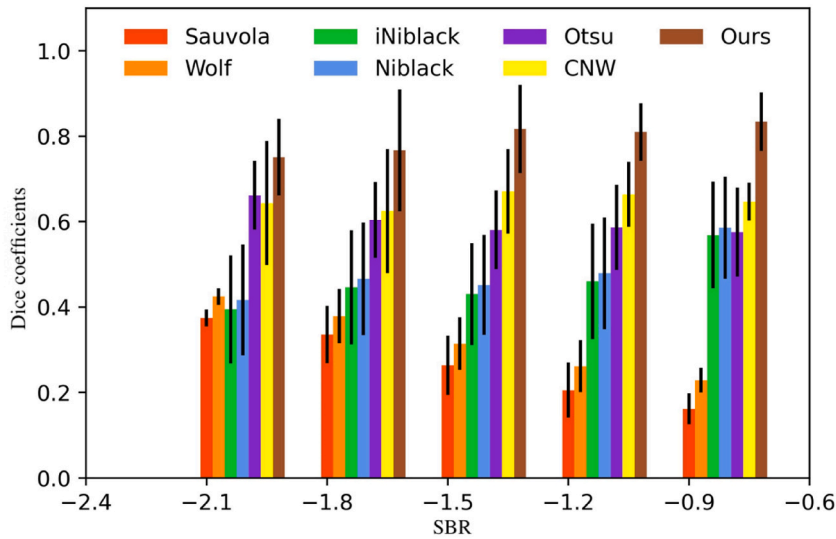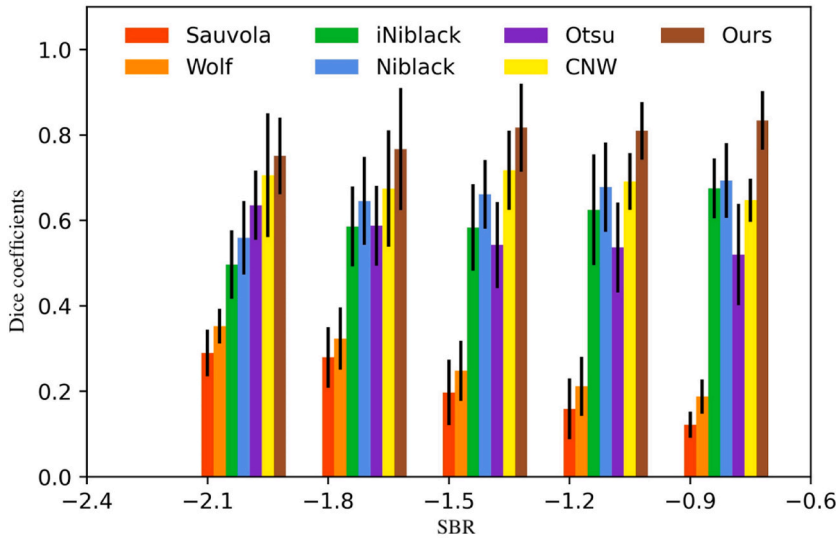
Fig. 10. (a), Original DSA image. (b), Ground truth. (c–h), Results by our method with different k values, 5, 10, 15, 20, 25, and 30, respectively.

(a)

(b)

Fig. 11. (a), Dice coefficients of different methods without post-processing at various SBRs. (b), Dice coefficients of the methods with post-processing.

robust and the advantage of local thresholding as being responsive to fine structures of an image. As a result, the method demonstrated superior performance as compared to existing techniques. Another advantage of the method is that it has a consistency performance with respect to the setting of the single parameter in it. Test results validated that the method is also robust with regard to the SBRs of images, an feature that is important in practice since that even images of the same type have different contrast.

We compared the new method with some widely used techniques, including a global thresholding method and adaptive local thresholding methods. Results showed that the new method outperformed the other methods in terms of extracting fine details about the foreground and avoiding over-segmentation of the image or creating excessive noise in the results.

As we observed from the experiments, local adaptive thresholding methods have a tendency to amplify local structures, even when such local structures are noise. This drawback is well avoided by the new method. Global thresholding methods like [11,13,14,29], on the other hand, have difficulties in segmenting pixels if their intensities fall in a gray-zone between the foreground and background. The new method can accurately segment such pixels. The proposed method does not explicitly remove noise from images. However, such noise can be well removed by post-processing, as shown in experiments.

Since the size of our dataset is relatively small at this stage and training deep learning models on this dataset did not yield
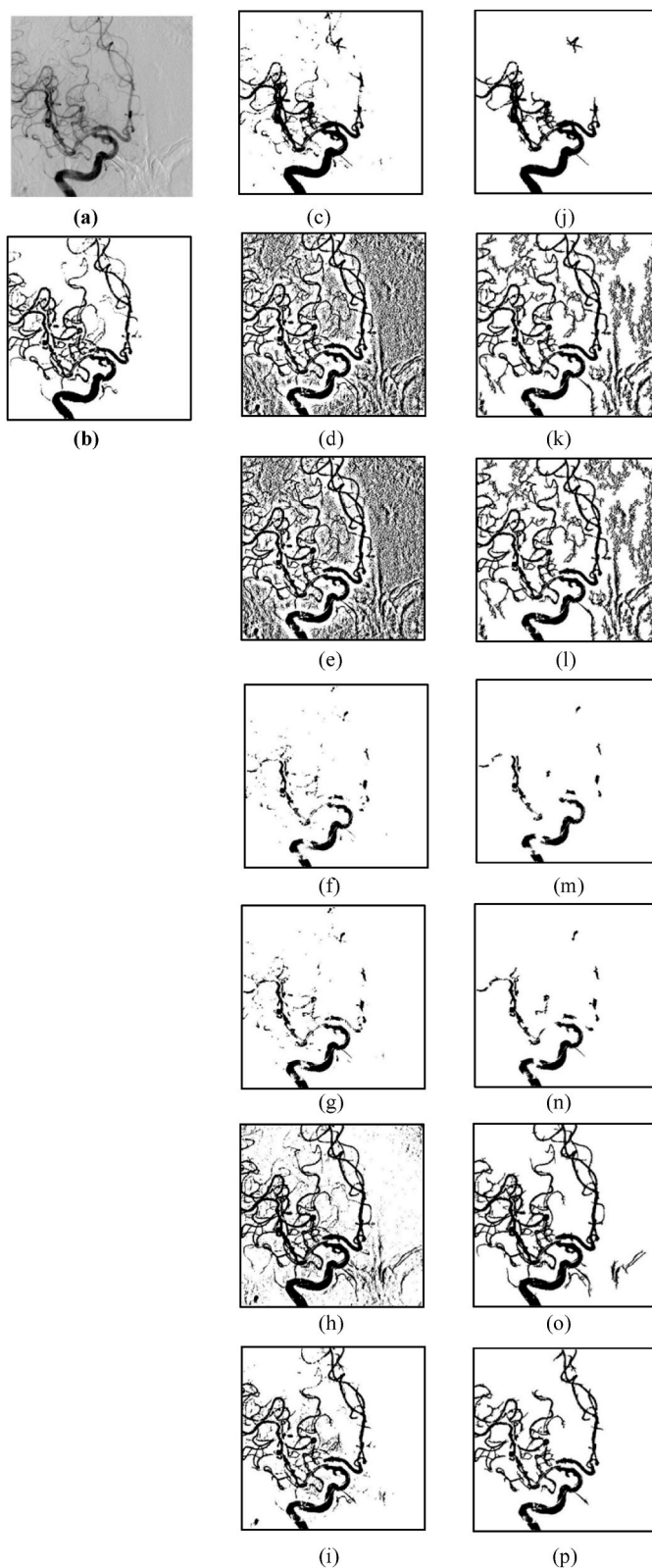
Fig. 12. (a), A DSA image at SBR of −2.1 dB. (b), Ground truth. (c–i), Results by Otsu, Niblack, iNiblack, Sauvola, Wolf, CNW, and our methods, respectively, without post-processing. (j–p), Corresponding results of (c–i) with post-processing.

Fig. 13. (a), A DSA image at SBR of −0.9 dB. (b), Ground truth. (c–i), Results by Otsu, Niblack, iNiblack, Sauvola, Wolf, CNW, and our methods, respectively, without post-processing. (j–p), Corresponding results of (c–i) with post-processing.
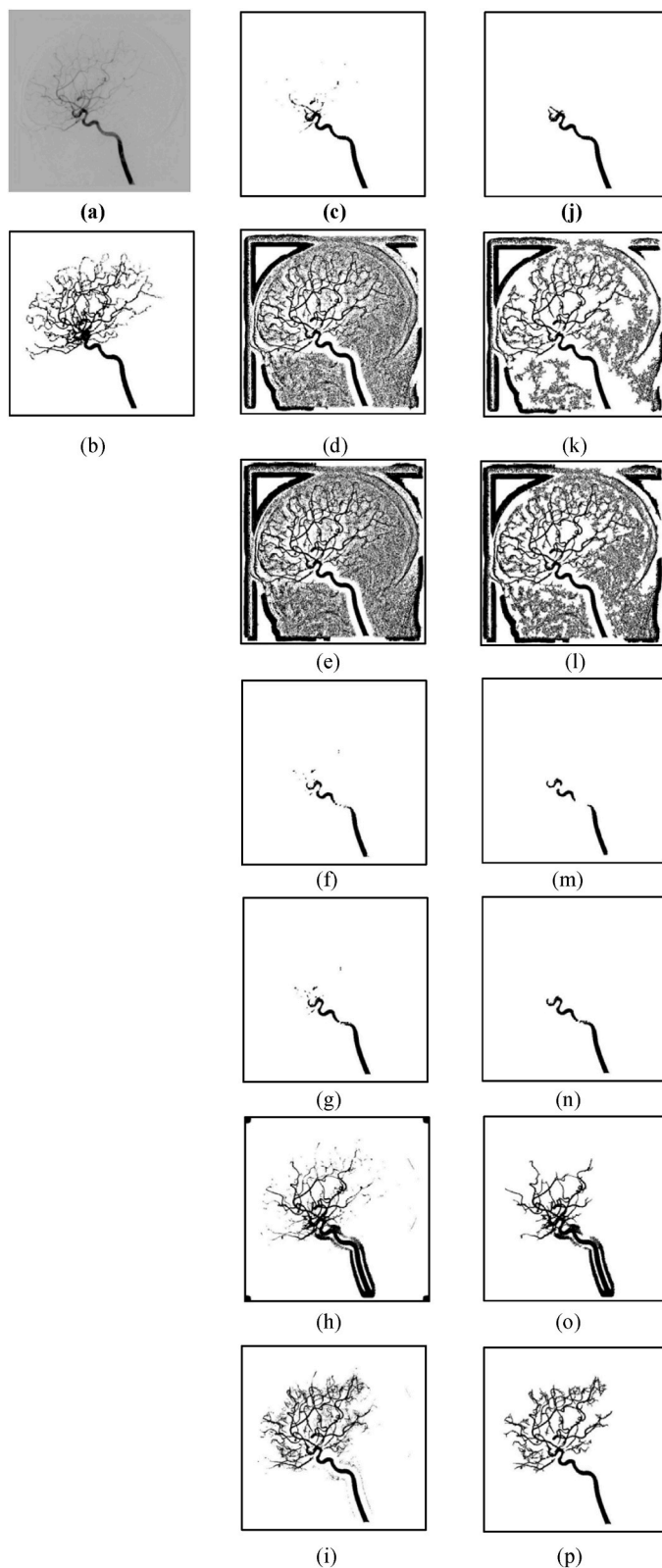
satisfactory segmentation results, we focus more on traditional image segmentation algorithms in this article. We are trying to communicate with several hospital units to establish a multi-data joint center, and in future we aim to further validate and improve our research results based on large-scale data.

Data availability

The data in this study were not included in any publicly available database. Data available on request from the authors due to privacy/ethical restrictions.

Ethics approval

This study was reviewed and approved by Clinical Research and Application Institutional Review Board of The Second Affiliated Hospital of Guangzhou Medical University with the approval number: No:2023-hg-ks-24, dated 2023-08-28.

CRediT authorship contribution statement

Min Zhang: Writing – review & editing, Writing – original draft, Formal analysis, Data curation. **Jun Wang:** Writing – review & editing, Writing – original draft, Formal analysis, Data curation. **Xinhua Cao:** Writing – review & editing, Writing – original draft, Software, Formal analysis. **Xiaoyin Xu:** Writing – review & editing, Writing – original draft, Project administration, Methodology, Conceptualization. **Jie Zhou:** Writing – review & editing, Writing – original draft, Resources, Data curation. **Huai Chen:** Writing – review & editing, Writing – original draft, Project administration, Methodology, Conceptualization.

Declaration of competing interest

All authors have no conflicts of interest to declare.

Appendix A. Supplementary data

Supplementary data to this article can be found online at https://doi.org/10.1016/j.heliyon.2024.e38579.

References

[1] Y. Luo, L. Sun, Digital subtraction angiography image segmentation based on multiscale Hessian matrix applied to medical diagnosis and clinical nursing of coronary stenting patients, Journal of Radiation Research and Applied Sciences 16 (3) (2023).
[2] W. Xu, et al., ERNet: edge regularization network for cerebral vessel segmentation in digital subtraction angiography images, IEEE Journal of Biomedical and Health Informatics 28 (3) (2024) 1472–1483.
[3] J.E. Exaire, J. Saw, C. Bajzer, Cerebrovascular angiography, in: Handbook of Complex Percutaneous Carotid Intervention, Springer, 2007, pp. 99–109.
[4] Y. Zhang, H. Jiang, L. Ma, Blood vessel segmentation based on digital subtraction angiography sequence, in: 2018 IEEE International Conference on Systems, Man, and Cybernetics (SMC), IEEE, 2018.
[5] P. Xiuqin, Q. Zhang, H. Zhang, S. Li, A fundus retinal vessels segmentation scheme based on the improved deep learning U-Net model, IEEE Access 7 (2019) 122634–122643.
[6] S.A. Kamran, K.F. Hossain, A. Tavakkoli, S.L. Zuckerbrod, K.M. Sanders, S.A. Baker, RV-GAN: segmenting retinal vascular structure in fundus photographs using a novel multi-scale generative adversarial network, in: International Conference on Medical Image Computing and Computer-Assisted Intervention, Springer, 2021.
[7] D. Adapa, A.N. Joseph Raj, S.N. Alisetti, Z. Zhuang, G. Naik, A supervised blood vessel segmentation technique for digital Fundus images using Zernike Moment based features, PLoS One 15 (3) (2020) e0229831.
[8] M. Zhang, C. Zhang, X. Wu, X. Cao, G.S. Young, H. Chen, X. Xu, A neural network approach to segment brain blood vessels in digital subtraction angiography, Comput. Methods Progr. Biomed. 185 (2020) 105159.
[9] C. Meng, K. Sun, S. Guan, Q. Wang, R. Zong, L. Liu, Multiscale dense convolutional neural network for DSA cerebrovascular segmentation, Neurocomputing 373 (2020) 123–134.
[10] A. Vepa, A. Choi, N. Nakhaei, W. Lee, N. Stier, A. Vu, G. Jenkins, X. Yang, M. Shergill, M. Desphy, Weakly-supervised convolutional neural networks for vessel segmentation in cerebral angiography, in: Proceedings of the IEEE/CVF Winter Conference on Applications of Computer Vision, 2022.
[11] N. Otsu, A threshold selection method from gray-level histograms, IEEE transactions on systems, man, and cybernetics 9 (1) (1979) 62–66.
[12] Y. Solihin, C. Leedham, Integral ratio: a new class of global thresholding techniques for handwriting images, IEEE Trans. Pattern Anal. Mach. Intell. 21 (8) (1999) 761–768.
[13] W. Niblack, An Introduction to Digital Image Processing, Strandberg Publishing Company, 1985.
[14] J. Sauvola, M. Pietikäinen, Adaptive document image binarization, Pattern Recogn. 33 (2) (2000) 225–236.
[15] B. Gatos, I. Pratikakis, S.J. Perantonis, Adaptive degraded document image binarization, Pattern Recogn. 39 (3) (2006) 317–327.
[16] P.V. Henstock, D.M. Chelberg, Automatic gradient threshold determination for edge detection, IEEE Trans. Image Process. 5 (5) (1996) 784–787.
[17] P.K. Sahoo, G. Arora, A thresholding method based on two-dimensional Renyi's entropy, Pattern Recogn. 37 (6) (2004) 1149–1161.
[18] J.N. Kapur, P.K. Sahoo, A.K. Wong, A new method for gray-level picture thresholding using the entropy of the histogram, Comput. Vis. Graph Image Process 29 (3) (1985) 273–285.
[19] Y. Xiao, Z. Cao, J. Yuan, Entropic image thresholding based on GLGM histogram, Pattern Recogn. Lett. 40 (2014) 47–55.
[20] S. Sarkar, S. Das, Multilevel image thresholding based on 2D histogram and maximum Tsallis entropy—a differential evolution approach, IEEE Trans. Image Process. 22 (12) (2013) 4788–4797.
[21] O.J. Tobias, R. Seara, Image segmentation by histogram thresholding using fuzzy sets, IEEE Trans. Image Process. 11 (12) (2002) 1457–1465.

[22] S. Agrawal, R. Panda, A. Abraham, A novel diagonal class entropy-based multilevel image thresholding using coral reef optimization, IEEE Transactions on Systems, Man, and Cybernetics: Systems 50 (11) (2018) 4688–4696.

[23] C. Wolf, J.-M. Jolion, Extraction and recognition of artificial text in multimedia documents, Formal Pattern Analysis & Applications 6 (4) (2004) 309–326.

[24] M.-L. Feng, Y.-P. Tan, Contrast adaptive binarization of low quality document images, IEICE Electron. Express 1 (16) (2004) 501–506.

[25] K. Khurshid, I. Siddiqi, C. Faure, N. Vincent, Comparison of Niblack inspired binarization methods for ancient documents, in: Document Recognition and Retrieval XVI, 2009. SPIE.

[26] K. Zhang, L. Zhang, K.-M. Lam, D. Zhang, A level set approach to image segmentation with intensity inhomogeneity, IEEE Trans. Cybern. 46 (2) (2015) 546–557.

[27] B. Wang, X. Gao, D. Tao, X. Li, A nonlinear adaptive level set for image segmentation, IEEE Trans. Cybern. 44 (3) (2013) 418–428.

[28] C. Zhang, Y. Xie, D. Liu, L. Wang, Fast threshold image segmentation based on 2D fuzzy Fisher and random local optimized QPSO, IEEE Trans. Image Process. 26 (3) (2016) 1355–1362.

[29] K. Saddami, K. Munadi, S. Muchallil, F. Arnia, Improved thresholding method for enhancing Jawi binarization performance, in: 2017 14th IAPR International Conference on Document Analysis and Recognition (ICDAR), IEEE, 2017.

[30] K. Saddami, P. Afrah, V. Mutiawani, F. Arnia, A new adaptive thresholding technique for binarizing ancient document, in: 2018 Indonesian Association for Pattern Recognition International Conference (INAPR), IEEE, 2018.